

# Quantitative imaging analysis of nanoparticles and dissolved forms using laser ablation-single particle-ICP-mass spectrometry

Shuji Yamashita<sup>1</sup>, Kumiko Ogawa<sup>2</sup>, Takafumi Hirata<sup>1\*</sup>

<sup>1</sup>Geochemical Research Centre, The University of Tokyo, 7-3-1 Hongo, Bunkyo-ku, Tokyo 113-0033, Japan

<sup>2</sup>Division of Pathology, National Institute of Health Sciences, 3-25-26 Tonomachi, Kawasaki-ku, Kawasaki, Kanagawa 210-9501, Japan

## Summary

Laser ablation-single particle-ICP-mass spectrometry (LA-spICP-MS) was applied to define the size, position of silver nanoparticles (Ag NPs), and the concentration of ionic Ag (dissolved Ag) on a frozen section of mouse liver (6 hours after intraperitoneal administered 60 nm Ag NPs (0.2 mg per mouse)). For the accurate size calibration of Ag NPs and quantitative analysis of ionic Ag, a cellulose filter paper doped with Ag NPs suspension and a custom-made photocurable resin reference material containing ionic Ag were prepared in this study. From the imaging results of liver sample, preferential accumulation of the Ag NPs in certain regions was observed. Ionic Ag was also accumulated at regions where Ag NPs are. This suggests that there is a possible contribution of dissolution of Ag NPs through cell activity. This is supported by the detection of small Ag NPs (8–20 nm). The simultaneous imaging analyses of both Ag NPs and ionic Ag can become a useful tool to understand the mechanism of incorporation or metabolism of the NPs.

**Key words:** nanoparticle, imaging analysis, quantitative analysis, laser ablation, single particle-inductively coupled plasma-mass spectrometry

**Statements about COI:** The authors declare no conflict of interest associated with this manuscript.

## Introduction

Various inorganic nanoparticles (NPs) are widely used in many research fields such as biochemical, material, and environmental sciences[1-3]. Among inorganic NPs, silver NPs (Ag NPs) are the major NPs found in cosmetics, deodorizer, electronic devices, and medicine[4-6]. In addition, Ag, either in ionic or particulate form, are well-known to exhibit strong antimicrobial activity[7,8].

Despite Ag NPs having remarkable physicochemical or biochemical features, these NPs can potentially bring risks to both human health and the environment[9].

Many biochemists are increasingly interested in the mechanism of toxicity of the NPs: how the NPs interact with cells, or what is the critical size of NPs that contribute to cytotoxicity. Smaller sized NPs can pass through the cell membrane[10], and it is widely believed that reactivities with cellular components such as nucleic acids, proteins, and fatty acids would increase in the small NPs due to their larger surface area. Recently, Cho *et al.*

---

### \*Correspondence:

Geochemical Research Centre, The University of Tokyo, 7-3-1

Hongo, Bunkyo-ku, Tokyo 113-0033, Japan

Tel: +81 3 5841 4621

E-mail: E-mail: [hrt1@eqchem.s.u-tokyo.ac.jp](mailto:hrt1@eqchem.s.u-tokyo.ac.jp)

---

Received: August 31, 2021

Accepted: November 18, 2021

Released online: January 6, 2022



This work is licensed under a Creative Commons Attribution 4.0 International License.

©2021 Yamashita S. *et al.*

evaluated the size-dependent toxicity of Ag NPs through intraperitoneal administration of Ag NPs of varying sizes (10, 60, and 100 nm) into BALB/c mice [11]. For the mice which were administered with 10 nm Ag NPs, a reduction in activity was observed, and histopathological changes such as congestion, vacuolation, single cell necrosis, and focal necrosis in the liver were also found. The size and the distribution of Ag NPs within the sample, can control the toxicity of the Ag NPs. To unveil the biological effects of the NPs, and also to investigate the mechanism of the removal of the NPs (*i.e.*, fate of the incorporated NPs), sensitive analytical techniques for imaging of both the elements and NPs are highly desired.

For the evaluation of toxicity and transport mechanisms of NPs, many analytical techniques such as optical and dark-field microscopy [12], scanning electron microscopy (SEM) [13], surface-enhanced Raman scattering (SERS) [14], and photothermal microscopy [15] have been widely used. For the elucidation of distribution of NPs, many analytical techniques including atomic force microscopy (AFM) or secondary ion mass spectrometry (SIMS) have been adopted [16]. However, these analytical techniques are not capable for quantitative imaging of both elements and NPs from biological tissue samples.

Recently, laser ablation-ICP-mass spectrometry (LA-ICP-MS) is described as a fast, sensitive, and quantitative analytical tool for in-situ elemental analysis or elemental imaging [17,18]. With the LA-ICP-MS, visualization of elemental distributions with spatial resolution in the  $\mu\text{m}$ -range can be achieved from biological tissues being  $>1$  mm. Moreover, LA-ICP-MS technique offers reliable quantitative data by using matrix-matched standard materials [19-21]. In recent years, ICP-MS technique designed for detection of single nanoparticle (single particle-ICP-MS: spICP-MS) technique is developed. With the spICP-MS technique, various information on the size, number concentrations, and elemental composition of the NPs can be derived [22,23]. By combining the spICP-MS technique and laser ablation sampling technique, rapid and sensitive imaging of NPs in solid samples can be made. Recent studies have demonstrated that the LA-spICP-MS has great potential for size and distribution analysis of NPs as well as imaging analysis of ionic form in biomaterials [24-26].

This study focuses on the establishment of an analytical methodology using the LA-spICP-MS for simultaneous determinations of (a) size of NPs, (b) concentrations of ionic form (dissolved form), and (c) distributions of NPs and ionic form in biological samples. To do this, the spatial distributions of Ag (NPs and ions) in frozen liver sections collected from a mouse was investigated using the LA-spICP-MS. For accurate calibrations of the size of Ag NPs, a cellulose filter paper, which mimics the matrix of biological tissue samples, containing size-calibrated Ag NPs were used. Moreover, for the determination of Ag concentration, a custom-made photocurable resin reference material containing ionic Ag was used. To evaluate the reliability of the resulting Ag concentration, the Ag concentration was separately measured by solution-based ICP-MS technique after the sample decomposition and dissolution procedures.

## Experimental section

### Preparation of tissue samples

Our previous study focused on the toxicity of Ag NPs on seven-week-old female BALB/c mice (body weight: 16.3–20.2 g) [11]. Details of the preparation of the tissue sample are as follows: citrate-coated Ag NPs of 60 nm ( $59.8 \pm 6.2$  nm) in diameter purchased from NanoComposix (San Diego, CA, USA) were used. 0.2 mg of the 60 nm Ag NPs were intraperitoneally injected in the mice. The mice were then anesthetized with isoflurane (Mylan Inc., Tokyo, Japan) 6 hours after administration. A liver sample from one mouse was resected and subjected to analysis. The total Ag concentration of part of its liver was measured by solution-based ICP-MS. The resulting Ag concentration of the liver sample for this analysis was  $35.8 \mu\text{g g}^{-1}$  [11].

The collected livers were stored at  $-80^\circ\text{C}$ . The frozen liver sample was embedded in optimal cutting temperature compound, and was sliced into 10- $\mu\text{m}$ -thick sections with a cryotome (Leica Microsystems, Wetzlar, Germany), and then placed on glass slides. No staining procedures were made on the analyzing sliced samples. There was an interval between the preparation of the sliced samples and the time of imaging analysis.

The major problem associated with the present LA-spICP-MS instrument is that the technique is not sensitive enough to monitor the size of the Ag NPs being diameters  $<10$  nm. To demonstrate the capability of the size analysis of the LA-spICP-MS technique, we focused the size and mapping analyses of 60 nm Ag NPs in the mouse liver tissues. Moreover, from the previous study, dark brown pigmentation in the thoracic lymph nodes was confirmed at 6 hours in the 60 nm administration group, suggesting that Ag NPs are in the lymphatic flow and bloodstream [11]. From this result, the mice administered with 60 nm Ag NPs after 6 hours was used for imaging analysis.

### Imaging analysis of the frozen section of mouse liver

Simultaneous imaging analysis of both the Ag NPs and ionic Ag was carried out by the LA-spICP-MS technique. The ICP-MS instrument used in this study was a magnetic sector-based ICP-MS (AttoM, Nu Instruments, Wrexham, UK). Neither isobaric nor polyatomic interferences were found on  $^{107}\text{Ag}^+$  signals ( $m/z$  of 107 u), mass resolving power of about 300 was used throughout the study to maximize the instrument sensitivity. Ag ions were detected by a pulse counting mode with an attenuator system. The attenuator system which can attenuate the ion flux down to about 1/500 level by passing through the platinum grid. This was done to ensure the ion beam with count rates of 50 Mcps is reduced to 100 kcps, obviating the risk of erroneous measurements due to the counting loss of analyte ions[27]. Switching on/off the attenuator device is made automatically within 1 ms, and thus, detection of ion beam with wider dynamic range covering 8 orders of magnitude (*i.e.*, from 1 to  $10^8$  cps) is achieved by the present system setup. The attenuator system is very important to extend the range of size analysis of NPs[28].

For the laser ablation, a Nd:YAG laser (FQSS-266Q, CryLas, Berlin, Germany) operating at UV wavelength (266 nm) with a pulse duration of 1 ns was employed. The laser operating conditions were set to fluence of  $0.4 \text{ J cm}^{-2}$ , repetition rate of 1 kHz, and ablation pit size of  $4 \mu\text{m}$ . Imaging analysis was made based on the repeated line profiling analysis with scanning speed of  $2 \mu\text{m s}^{-1}$  and  $0 \mu\text{m}$  for the distance between the lines. In this study, a low laser fluence (*i.e.*,  $<1 \text{ J cm}^{-2}$ ) was adopted because of smaller contribution of the disintegration of NPs[25,29,30]. The laser induced sample aerosols were transported into the ICP with a mixed flow of He and Ar gases (He flow rate:  $0.7 \text{ L min}^{-1}$ , Ar flow rate:  $0.85 \text{ L min}^{-1}$ ).

The instrument was operated in time resolved analysis mode of an output signal intensity (cps) versus time. The duration time for each line was set at 50 s, with a dwell time of  $50 \mu\text{s}$  per reading. The signal intensity data obtained by the spICP-MS system were stored in the csv format. The resulting time-dependent signal intensity profiles were converted to the position-dependent signal intensity data based on the elapsed time and the raster rate, and then, the distributions of NPs and ionic form were visualized using in-house imaging software “iQuantNP”[24].

### Separation of signals from NPs and ionic forms

For the separation of signals originating from Ag NPs and signals from ionic Ag, discrimination level (threshold) was defined. Threshold of  $\mu + n\sigma$  ( $\mu$ : mean of the whole dataset,  $n$ : an integer multiple times (3 or 5), and  $\sigma$ : standard deviation) was used[23,31]. For the imaging analysis, however, this approach cannot be applied because the contents of Ag can vary largely within the samples. Recently, Metarapi *et al.* reported guidelines for analysis of NPs using LA-spICP-MS by processing the computational data via an “outlier” filter to differentiate between metal NPs and dissolved form[25,32]. In this study, referring to this reported protocol, the particle events were identified apart from instrumental background or dissolved form applying a moving median filter that replaces each data point in the raw data with the median of a certain number of adjacent data points. The threshold was calculated based on counting statistics in each median data point  $S$ , associated with the counts in the time slice:  $S + 5\sqrt{S}$ .

### Size calibration of NPs

For an accurate size analysis for NPs, a matrix-matched size calibration standard material is required[25,33,34]. For most biological samples, the main component is carbon. Thus, we have selected a cellulose filter paper to prepare the matrix-matched size calibration standard material. Commercially available citrate-coated 60 nm Ag NPs ( $59 \pm 6 \text{ nm}$ ) from NanoComposix (San Diego, CA, USA) was used. A  $100 \mu\text{L}$  of solution containing Ag NPs with the number concentration of  $1.8 \times 10^{10} \text{ particles mL}^{-1}$  was dropped onto the cellulose filter paper (qualitative filter paper No. 1, ADVANTEC, Tokyo, Japan). The Ag NPs solution was left to dry for 1 hour at room temperature, and then used for size calibration. The aggregation of citrate-coated Ag NPs can occur in a biological solution, and thus, the sample matrix containing Gamble’s solution[35,36] or artificial lysosomal fluid buffer[35,36] was not used in this study.

The measured ion counts from single particle event reflect the total mass (*i.e.*, total number of Ag atoms) of the NPs, and thus, the size of the NPs can be calculated by the total ion counts of single particle events. The size of NPs was calibrated based on comparing the total ion counts of single NPs and those for the size standard material (60 nm Ag NPs)[37]. Hence, the size of Ag NPs was calculated based on the assumption that the Ag NPs present in the cell tissues had spherical shape. Total ion counts of the individual particle events were calculated by integrating the ion counts between starting and terminal channels[38]. The calibration factor was defined by the mean ion counts of single particle events obtained from about 1000 particles.

### Matrix-matched reference material for quantitative imaging analysis of ionic Ag

For the quantitative imaging analysis of ionic Ag, a matrix-matched reference material was prepared. In this study, a photocurable resin was used. Photocurable resins have advantages as follows; (a) including carbon as a major component, (b) easy handling, and (c) long shelf life. About 6  $\mu\text{L}$  of 1000  $\text{mg L}^{-1}$  of silver atomic absorption standard solution ( $\text{AgNO}_3\cdot\text{HNO}_3$  (0.1  $\text{mol L}^{-1}$ ), Kanto Chemical Co., Inc., Tokyo, Japan) was diluted by 100  $\mu\text{L}$  of ethanol, and then, 10  $\mu\text{L}$  of the diluted solution was added to 100 mg of the photocurable resin (Acryl-one type:# 2100N, Maruto Instrument Co., Ltd, Tokyo, Japan). The resulting mixture of photocurable resin and Ag solution was mixed well with the stirrer for 5 minutes for homogenization. Then, about 1 mg of the resulting mixture resin were dropped onto glass slides, and then pressed by another glass slide to make thin films. The pressed mixture resins were then left for 1 hour for polymerization under a lamp. The resulting calibration reference materials were square-shaped films with a size of 10 mm with a thickness of ca. 10  $\mu\text{m}$ .

The homogeneity of Ag resin reference material was evaluated by laser ablation of  $1000 \times 1000 \mu\text{m}$  through the laser ablation with fluence of  $6.3 \text{ J cm}^{-2}$ , repetition rate of 1 kHz, scanning speed of  $100 \mu\text{m s}^{-1}$ , repeated 15 line scans, and dwell time of 0.2 s. The resulting RSD value was 4.8%, and this is significantly smaller than the uncertainties in the spot analysis (e.g., 10%) achieved in this study.

Validation of Ag concentration in the resulting reference material was carried out with the solid mixing calibration using a multiple spot-LA-ICP-MS[39]. For the calibration using the solid mixing, an ultraviolet femtosecond laser equipped with a galvanometric scanner (wavelength of 257 nm; pulse duration of 290 fs: Jupiter Solid Nebulizer, ST Japan INC., Tokyo, Japan) coupled to a triple quadrupole-based ICP-MS (iCAP TQ, Thermo Fisher Scientific, Bremen, Germany) was used. Glass standard reference material NIST SRM 612 and NIST 614 SRM were used as calibration standards. Laser sampling from wide area with short time duration (0.1 s) was conducted with both the high repetition rate (10 kHz) and fast laser scan achieved by the Galvano scanner. Ablation pit size of 10  $\mu\text{m}$  with fluence of  $6.3 \text{ J cm}^{-2}$  was used here. Signal intensity data were acquired through 100 cycles repeated ablation from same area. The total ablated zone in three solid materials was  $100 \times 700 \times 1 \mu\text{m}$  for both the NIST SRM 612 and 614, and  $100 \times 700 \times 7 \mu\text{m}$  for photocurable resin reference material. Solid mixing was conducted by fast switching of the laser ablation (<1 ms) with high-repetition rate laser (10 kHz) on three materials: the resin and two NIST glass standard materials. The mixing ratios of three materials were controlled with the number of laser shots onto the solid materials. Total time for the laser ablation was fixed at 10 seconds, and stable signal intensities for 8 s were integrated, and the resulting signal data were used for further calculations. The nominal photocurable resin was calculated to contain  $7.75 \pm 0.42 \mu\text{g g}^{-1}$  of Ag.

### Calibration of ionic Ag concentration

Concentration of the ionic Ag ( $\mu\text{g g}^{-1}$ ) in the frozen section of mouse liver can be calibrated by signal intensity ( $I$  in counts), volume of ablation zone ( $V$  in  $\text{cm}^3$ ), and the density ( $\rho$  in  $\text{g cm}^{-3}$ ) of the resin and liver sample using Eq. (1):

$$C_{\text{sample}} = C_{\text{standard}} \times \frac{I_{\text{sample}}}{I_{\text{standard}}} \times \frac{V_{\text{standard}}}{V_{\text{sample}}} \times \frac{\rho_{\text{standard}}}{\rho_{\text{sample}}} \quad (1)$$

The main composition of the photocurable resin was triethylene glycol dimethacrylate, hence the  $\rho_{\text{standard}}$  was estimated to be  $1.1 \text{ g cm}^{-3}$ . In contrast, density of the biological samples can vary remarkably among the samples and/or positions. Typical density values of the biological samples are  $1.06 \text{ g cm}^{-3}$  for muscle,  $0.902 \text{ g cm}^{-3}$  for fat,  $1.03 \text{ g cm}^{-3}$  for blood, and  $1.05 \text{ g cm}^{-3}$  for cell[40,41], suggesting that the density can change about 10% among tissues and analysis points. In-situ and non-destructive analysis of density directly from the frozen sample is difficult, and thus, we take the density of liver tissues ( $\rho_{\text{sample}}$ ) as  $1.00 \text{ g cm}^{-3}$  as a representative value. The volumes of ablation zone for samples ( $V_{\text{sample}}$ ) were calculated by the resulting volume of ablation zone based on length, width, and depth of the ablation zone, whereas the volume of standard ( $V_{\text{standard}}$ ) was calculated based on the measured area ( $100 \times 300 \mu\text{m}$ ), and depth (2.3  $\mu\text{m}$ ) using the digital microscope (Leica VZ 700C, Leica Microsystems, Wetzlar, Germany).

## Results and discussion

### Evaluation for occurrence of disintegration of NPs with low laser fluence

To obtain accurate size data of Ag NPs in solid samples, disintegration of the Ag NPs during laser ablation was carefully

investigated in this study. The signal intensity (counts) of each particle event was converted into cubic root of the signal intensity ( $\text{counts}^{1/3}$ ). The measured size of the NPs should be correlated with cubic root of the total counts ( $\text{counts}^{1/3}$ ) for individual particle events.

The signal intensity distribution obtained from 60 nm Ag NPs using solution-based spICP-MS is shown in **Figure 1** (gray columns). The average signal intensity and variations defined as two standard deviations were  $8.0 \pm 3.0 \text{ counts}^{1/3}$  ( $N = 4703$ ). The resulting signal intensity distribution obtained by the LA-spICP-MS technique is also given in **Figure 1** as black columns. The 60 nm Ag NPs placed on the cellulose filter paper were measured by the LA-spICP-MS technique. The very low laser fluence of  $0.4 \text{ J cm}^{-2}$  was adopted. The average signal intensity and variations (2SD) were  $8.3 \pm 3.6 \text{ counts}^{1/3}$  ( $N = 1173$ ). For an easier

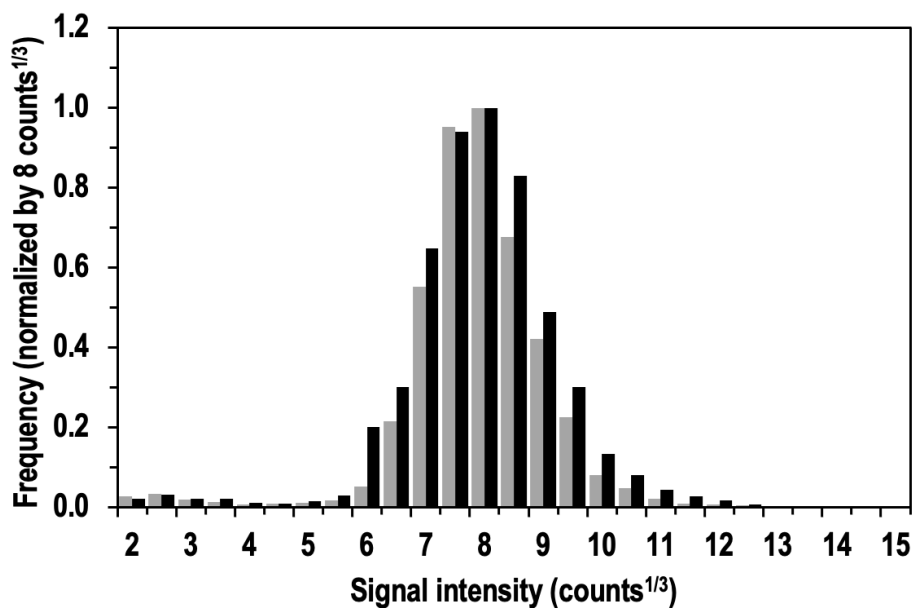


**Figure 1.** Signal intensity distributions obtained from 60 nm Ag NPs using solution-based spICP-MS (gray columns) and LA-spICP-MS (black columns).

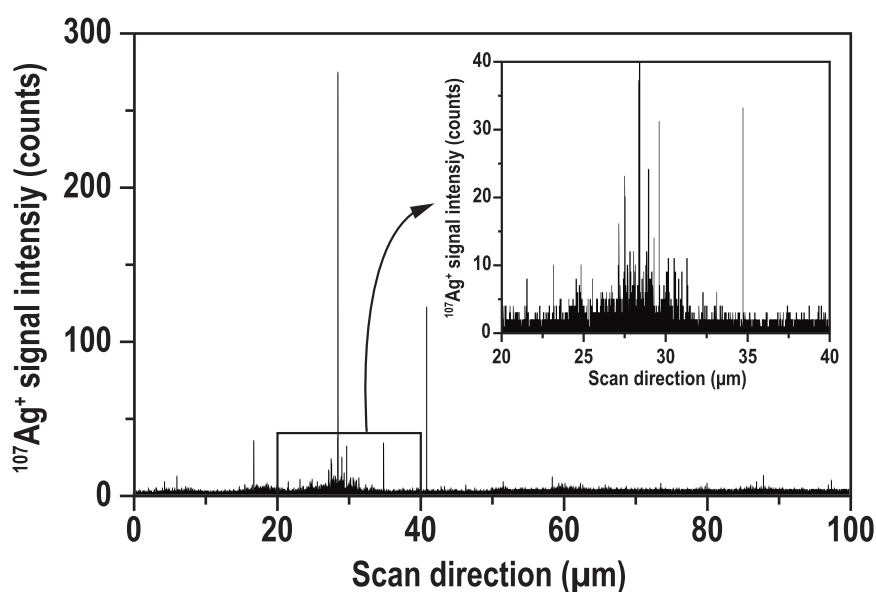


**Figure 2.** Single line scan data obtained from the second line of the mouse liver (marked with white arrows in Figs. 3(A)–3(I)).

comparison, the frequency normalized by  $8 \text{ counts}^{1/3}$ , rather than the absolute number of particles. The results demonstrated that the LA-spICP-MS technique was in good agreement with the solution-based spICP-MS within analytical uncertainty. The distribution pattern obtained by the LA-spICP-MS technique did not vary significantly from that obtained by the solution-based spICP-MS technique. Moreover, no significant increase in the Ag NPs with smaller signal intensities ( $<5 \text{ counts}^{1/3}$ ) can be found, suggestive of very small contribution of laser-induced disintegration through laser ablation sampling with low fluence.

### Simultaneous imaging analysis of Ag NPs and ionic Ag

**Figure 2** shows the signal intensity profile obtained from the second line of the mouse liver (marked with white arrows in **Figure 3(A)–3(I)**). The pulsed signal and low signal intensity data (baseline) represent particle and ionic form of Ag, respectively. This data suggests that the ionic forms of Ag were present around the NPs. In this study, data acquisition was conducted through line profiling analysis under the ablation pit size of  $4 \mu\text{m}$ , scanning speed of  $2 \mu\text{m s}^{-1}$ , and no gap between the lines. Under these conditions, size of the image (henceforth, we refer this as pixel) was  $1 \mu\text{m}$  in horizontal (x) and  $4 \mu\text{m}$  in vertical (y) directions. This high spatial resolution enables the detection of NPs and ions in cells.

The resulting concentration of ionic Ag, together with locations of ionic Ag were visualized by the iQuantNP software. **Figure 3(A)** illustrates the photographic image of the unstained frozen section of the mouse liver, and **Figure 3(B)** shows the distribution and concentration of ionic Ag, calculated based on eq. (1). The color reflects the concentration of ionic Ag as shown in the color bar (**Figure 3(B)**). The ionic Ag concentration in the frozen section of mouse liver varied from 1 to  $70 \mu\text{g g}^{-1}$  per pixel. The overall averaged Ag concentration calculated based on the total signal counts from Ag NPs and ionic Ag, was  $30.2 \mu\text{g g}^{-1}$ , and this is consistent with the bulk Ag content which were separately measured by solution-based ICP-MS technique through chemical decomposition and dissolution processes (*i.e.*,  $35.8 \mu\text{g g}^{-1}$ ). It is noted that the measured Ag concentration was different, reflecting sampling volume or weight through laser ablation. The variation of volume of ablation zone was not greater than 6% for the fabricated reference material. Moreover, since the sliced sample was ablated totally in this study, the ablation depth can be kept constant ( $10 \mu\text{m}$ ). Therefore, the variation of volume of ablation zone cannot account for the discrepancy in the Ag concentrations (*i.e.*, 17%) obtained by the solution-based ICP-MS ( $35.8 \mu\text{g g}^{-1}$ ) and LA-spICP-MS ( $30.2 \mu\text{g g}^{-1}$ ) techniques. Another possible explanation of the discrepancy is a density of the biological samples. Typical densities for muscle, fat, blood, and whole cell, were about  $1.06 \text{ g cm}^{-3}$ ,  $0.90 \text{ g cm}^{-3}$ ,  $1.03 \text{ g cm}^{-3}$ , and  $1.05 \text{ g cm}^{-3}$ , respectively [40,41], demonstrative of nearly 15% variations. In this study, the bulk Ag concentrations were calculated by assuming that the  $\rho_{\text{sample}}$  being  $1.00 \text{ g cm}^{-3}$  as a representative value of the whole tissues, and thus, the Ag concentration obtained the solution-based ICP-MS involved principal uncertainties being  $>15\%$ . We believe that the present discrepancy in the measured Ag concentrations using the solution-based ICP-MS and LA-spICP-MS techniques can be attributed to the empirical assumption that there was no variation in the density of the sample.

The good agreement with the measured Ag content through the imaging analysis and bulk analysis suggests that the calibration protocol based on the photocurable resin standard material is very promising for the quantitative imaging analysis. Moreover, the heterogeneous distribution of the ionic Ag found in the resulting imaging data suggests that the ionic Ag accumulates preferentially in certain region within the liver tissue (*e.g.*, sinusoid, Kupffer cell, or hepatocyte). This finding was consistent with histopathological feature, demonstrating detection of black granular pigment deposition (*i.e.*, Ag NPs) in the cytoplasm of Kupffer cells along the sinusoids in H&E-stained sections [11].

The imaging results of Ag NPs of various sizes are shown in **Figure 3(C)–3(I)**, in increments of 10 nm. A single Ag particle was indicated as a yellow-dot. Although the size of the dots is linearly correlated with the size of Ag NPs, the size of the dots does not reflect the actual size of Ag NPs. The only exception is the imaging results for Ag NPs of 8–20 nm. The color of the 8–20 nm Ag NPs image (**Figure 3(C)**) represents number of NPs per pixel. In **Figure 3(D)–3(I)**, imaging results of ionic Ag, as well as yellow dots for the Ag NPs, were also shown in gray-colored scale in background. Several interesting features can be derived through the comparison of the resulting images of ionic Ag and Ag NPs. First of all, the number of the smaller size Ag NPs increased. Second point is the heterogeneous distribution of both the ionic Ag and Ag NPs within the liver tissue. The ionic Ag and Ag NPs showed similar distribution patterns within the sample. Concentration of ionic Ag were high at areas where Ag NPs were enriched. From the **Figure 3 (C)** and **(D)** data (*i.e.*, imaging data of 8–20nm and 20–30 nm Ag NPs, respectively), these sizes distributed more densely and widely than the other sizes. This suggests that Ag NPs smaller than 30 nm can be incorporated in not only Kupffer cells in the sinusoids, but also hepatocytes.

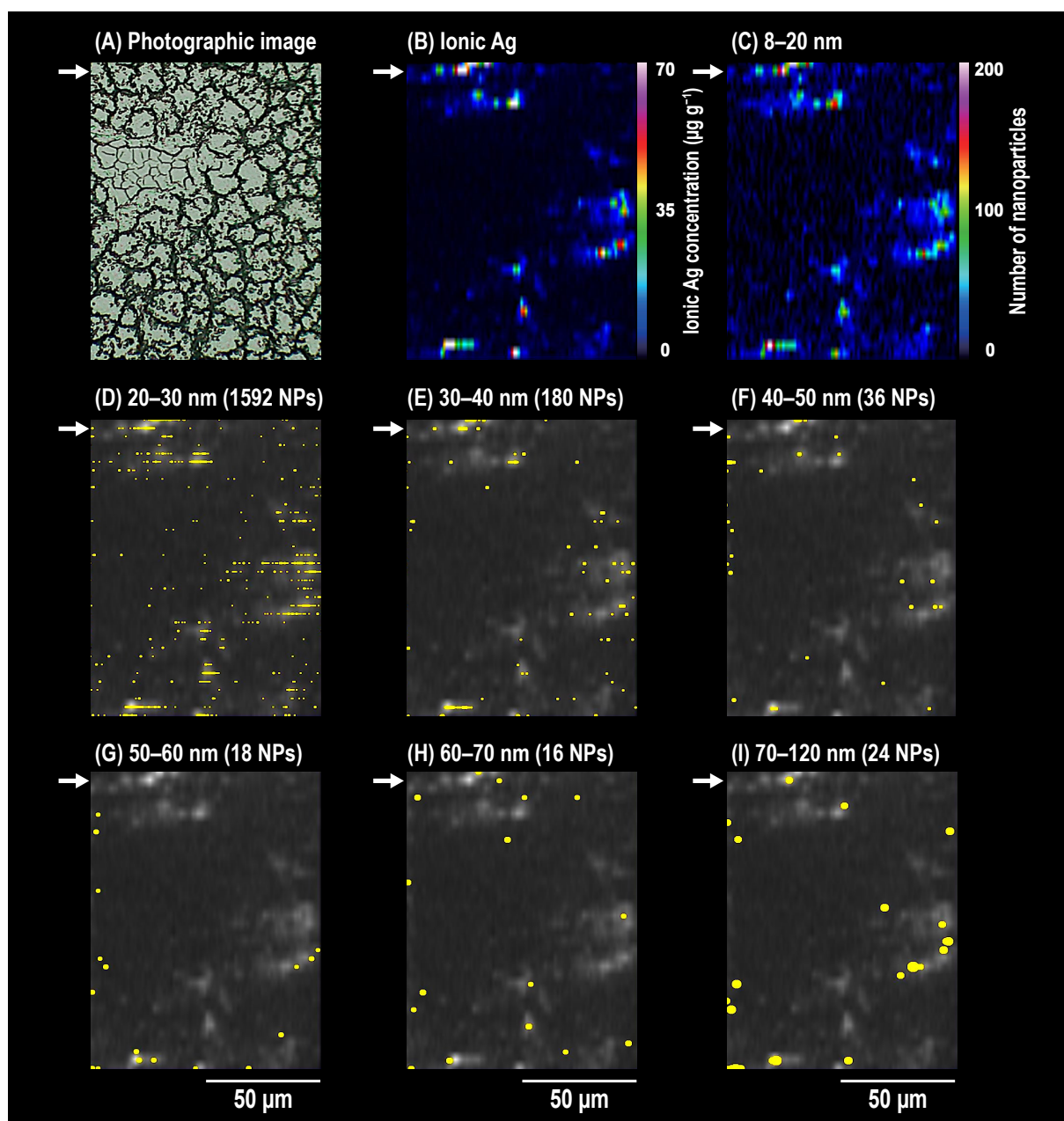


**Figure 3.** Resulting imaging data for both the ionic Ag and Ag NPs. (A) Photographic image of the frozen section of mouse liver (administered 60 nm Ag NPs (0.2 mg per mouse)). (B) Mapping data of the ionic Ag. (C)–(I) Resulting distribution images of Ag NPs for size range from  $\geq 8$  nm to  $< 120$  nm, in increments of 10 nm. Background color represents the gray-colored scale of (B) ionic Ag data. In figure (C), the color reflects the number of NPs per pixel. In figure (D)–(I), the yellow-dot represents the single Ag NP.

**Figure 4** illustrates the size distribution of Ag NPs found in the frozen section of mouse liver. The inserted figure shows the enlarged-scale of size distribution of the Ag NPs for size range of 40–120 nm. The measured sizes of the Ag NPs were significantly smaller than the administrated Ag NPs ( $59.8 \pm 6.2$  nm). The number of detected small particles ( $< 20$  nm) were  $> 1,000$  times higher than the number of 60 nm Ag NPs. The most plausible explanation for the detection of Ag NPs is that this is due to dissolution of Ag NPs through cellular activity. Moreover, the size distribution data also revealed the presence of the Ag NPs with larger sizes (*e.g.*,  $> 60$  nm). A wide size distribution of the detected Ag NPs in the liver tissue suggests there are both the dissolution and aggregation of the Ag NPs occurring in the tissue.

Imaging and size distribution data (**Figure 3** and **4**) revealed the accumulation of Ag NPs and ionic Ag in certain positions of

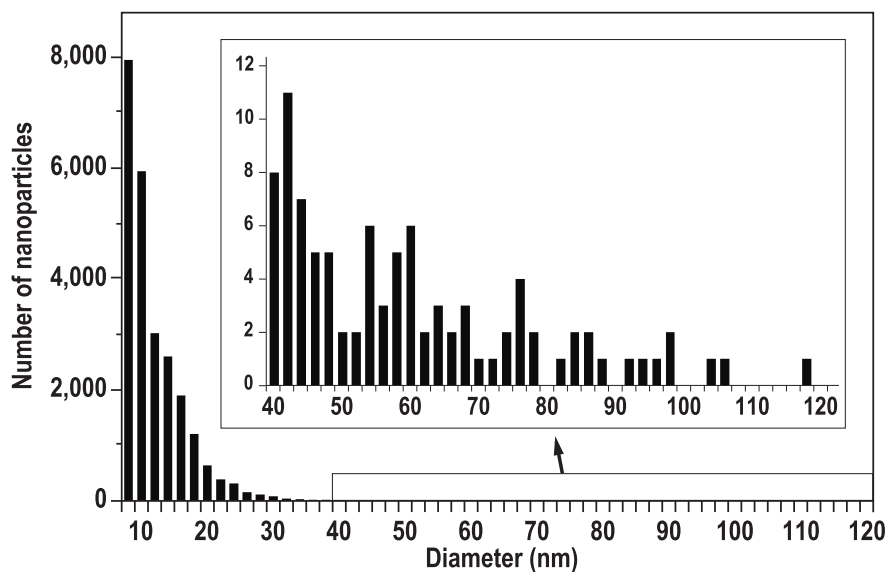


**Figure 4.** Measured size distribution for Ag NPs obtained from the frozen section of mouse liver (administered 60 nm Ag NPs ( $59.8 \pm 6.2$  nm)). The insert shows the size distribution of the Ag NPs for size range from 40–120 nm.

the liver. These data suggest that the Ag NPs is likely to be dissolved through cell activity. Singh *et al.* reported that Ag NPs were internalized via scavenger receptor-mediated phagocytic uptake and trafficked into the cytoplasm in macrophages [42]. After the incorporation of Ag NPs into the cells, Ag NPs degrades within the cells to release ionic Ag. Navarro *et al.* also reported that  $\text{H}_2\text{O}_2$ , a metabolite of algae, reacts with Ag NPs to form hydroxyl radicals and this forms ionic Ag as a byproduct [43]. However, there is no clear evidence on the region where the occurrence of Ag NPs dissolution after intraperitoneal administration. It is feasible that the dissolution of Ag NPs could have occurred by the time Ag NPs reached the liver. As for the aggregation of Ag NPs, the aggregation of the Ag NPs can occur under exposure to acidic environment and/or with high ionic strength containing divalent cations (*e.g.*,  $\text{Ca}^{2+}$ ) [44,45]. These can be the cause of agglomeration of Ag NPs observed in this frozen section of mouse liver.

Previous studies reported that NPs, which are not immediately trapped by Kupffer cells, are translocated through the fenestrated vascular endothelium into the Dissé spaces to be taken up by hepatocytes and processed into biliary canaliculi [46]. Hirn *et al.* observed through transmission electron microscopy (TEM) that 18 nm Au NPs were predominantly found in not only Kupffer cells, but also endothelial cells and hepatocyte [47]. They also reported that both the small and large agglomerates of Au NPs were observed in Kupffer cells. From this research, Ag NPs can be incorporated into the Kupffer cells and hepatocytes. Despite these observations, the mechanisms of accumulation of NPs in hepatocytes remain unclear. For future studies, we hope that the LA-spICP-MS technique can provide important clues to understand the mechanism of metabolic process of the Ag NPs in the liver tissue.

## Conclusion

Simultaneous determinations of (a) size of Ag NPs, (b) concentrations of ionic Ag (dissolved form), and (c) distributions of both the Ag NPs and ionic Ag in a frozen section of mouse liver was carried out by the spICP-MS coupled with laser ablation sampling technique. The size of Ag NPs was calibrated by a matrix-matched reference material prepared through the addition of NPs suspension onto a cellulose filter paper. For the quantitative analysis of Ag concentration, a calibration reference material using the photocurable resin spiked with the ionic Ag ( $7.75 \pm 0.42 \mu\text{g g}^{-1}$ ) was used. The resulting Ag concentration obtained by averaging the overall analysis area was  $30.2 \mu\text{g g}^{-1}$ . This was consistent with the bulk concentration (*i.e.*,  $35.8 \mu\text{g g}^{-1}$ ) obtained by solution-based ICP-MS technique, suggestive of high reliability of the present analysis protocol.

The imaging data of the frozen section of mouse liver showed that both the ionic Ag and Ag NPs were heterogeneously distributed within the liver tissue. The number of the smaller size Ag NPs increased. Another important information derived from the imaging data was the similarity between the distribution of ionic Ag and the distribution of the Ag NPs, suggesting that

the Ag NPs can be dissolved through cell activity. This is also supported by the changes in the size distribution of the Ag NPs. Moreover, based on the size distribution of the Ag NPs, both the dissolution and aggregation has occurred. The data obtained in this study demonstrate that the combination of two high spatial resolution images of both the NPs and ionic forms using the LA-spICP-MS technique can provide key information concerning the transport, interaction, and decomposition features of the NPs.

## Acknowledgement

We are grateful to Tetsuya Tamaki (Next Lab, Tokyo, Japan) for technical supports. We are also grateful to Hui Hsin Khoo (The Univ. of Tokyo) for scientific advice and critical reading of the manuscript. This work was financially supported by a Grant-in-Aid for Scientific Research (JP19H01081 and JP 21H04511) from the Ministry of Education, Culture, Sports, Science and Technology, Japan.

## References

- [1] Kessler R: Engineered nanoparticles in consumer products: understanding a new ingredient. *Environ Health Perspect* 119(3): A120-A5, 2011.
- [2] Weir A, Westerhoff P, Fabricius L, Hristovski K, Van Goetz N: Titanium Dioxide Nanoparticles in Food and Personal Care Products. *Environ. Sci. Technol* 46: 2242-2250, 2012.
- [3] Wei Y, Yan B: Nano products in daily life: to know what we do not know. *Natl. Sci. Rev* 3: 414-415, 2016.
- [4] Ahamed M, Alsalmi MS, Siddiqui MK: Silver nanoparticle applications and human health. *Clin Chim Acta* 411: 1841-1848, 2010.
- [5] Larginho M, Baptista PV: Gold and silver nanoparticles for clinical diagnostics—From genomics to proteomics. *J. Proteomics* 758(10): 2811-2823, 2012.
- [6] Schluesener JK, Schluesener HJ: Nanosilver: application and novel aspects of toxicology. *Arch Toxicol* 87: 569-576, 2013.
- [7] Mijndonckx K, Leys N, Mahillon J, Silver S, Van Houdt R: Antimicrobial silver: uses, toxicity and potential for resistance. *Biometals* 26: 609-621, 2013.
- [8] Morones JR, Elechiguerra JL, Camacho A, Holt K, Kouri JB, Ramirez JT, Yacaman MJ: The bactericidal effect of silver nanoparticles. *Nanotechnology* 16: 2346-2353, 2005.
- [9] Schäfer B, Brocke JV, Epp A, Götz M, Herzberg F, Kneuer C, Sommer Y, Tentschert J, Noll M, Günther I, Banasiak U, Böhl GF, Lampen A, Luch A, Hensel A: State of the art in human risk assessment of silver compounds in consumer products: a conference report on silver and nanosilver held at the BfR in 2012. *Arch Toxicol* 87: 2249-2262, 2013.
- [10] Pan Y, Neuss S, Leifert A, Fischler M, Wen F, Simon U, Schmid G, Brandau W, Jahnen-Dechent W: Size-dependent cytotoxicity of gold nanoparticles. *Small* 3: 1941-1949, 2007.
- [11] Cho YM, Mizuta Y, Akagi JI, Toyoda T, Sone M, Ogawa K: Size-dependent acute toxicity of silver nanoparticles in mice. *J. Toxicol. Pathol* 31: 73-80, 2018.
- [12] Aaron J, Travis K, Harrison N, Sokolov K: Dynamic imaging of molecular assemblies in live cells based on nanoparticle plasmon resonance coupling. *Nano Lett* 9(10): 3612-3618, 2009.
- [13] Beveridge JS, Stephens JR, Williams ME: Differential magnetic catch and release: experimental parameters for controlled separation of magnetic nanoparticles. *Analyst* 136(12): 2564-2571, 2011.
- [14] Kneipp J, Kneipp H, Rice WL, Kneipp K: Optical probes for biological applications based on surface-enhanced Raman scattering from indocyanine green on gold nanoparticles. *Anal Chem* 77(8): 2381-2385, 2005.
- [15] Nam J, Won N, Jin H, Chung H, Kim S: pH-induced aggregation of gold nanoparticles for photothermal cancer therapy. *J Am Chem Soc.* 131(38): 13639-13645, 2009.
- [16] Mourdikoudis S, Pallares RM, Thanh NTK: Characterization techniques for nanoparticles: Comparison and complementarity upon studying nanoparticle properties. *Nanoscale* 10: 12871-12934, 2018.
- [17] Reifschneider O, Wehe CA, Raj I, Ehmcke J, Ciarimboli G, Sperling M, Karst U: Quantitative bioimaging of platinum in polymer embedded mouse organs using laser ablation ICP-MS. *Metallomics* 5: 1440-1447, 2013.
- [18] Limbeck A, Galler P, Bonta M, Bauer G, Nischkauer W, Vanhaecke F: Recent advances in quantitative LA-ICP-MS analysis: challenges and solutions in the life sciences and environmental chemistry. *Anal Bioanal Chem* 407: 6593-6617, 2015.
- [19] Zoriy M, Matusch A, Spruss T, Becker JS: Laser ablation inductively coupled plasma mass spectrometry for imaging of copper, zinc, and platinum in thin sections of a kidney from a mouse treated with cis-platin. *Int. J. Mass Spectrom* 260(2): 102-106, 2007.
- [20] Šala M, Šelih VS, Van Elteren JT: Gelatin gels as multi-element calibration standards in LA-ICP-MS bioimaging: fabrication of homogeneous standards and microhomogeneity testing. *Analyst* 142: 3356-3359, 2017.
- [21] Köppen C, Reifschneider O, Castanheira I, Sperling M, Karst U, Ciarimboli G: Quantitative imaging of platinum based on laser

- ablation-inductively coupled plasma-mass spectrometry to investigate toxic side effects of cisplatin. *Metallomics* 7(12): 1595-1603, 2015.
- [22] Degueldre C, Favarger PY: Colloid analysis by single particle inductively coupled plasma-mass spectroscopy: a feasibility study. *Colloids Surfaces A Physicochem. Eng. Asp* 217(1-3): 137-142, 2003.
- [23] Pace HE, Rogers NJ, Jarolimek C, Coleman VA, Higgins CP, Ranville JF: Determining transport efficiency for the purpose of counting and sizing nanoparticles via single particle inductively coupled plasma mass spectrometry. *Anal. Chem* 83: 9361-9369, 2011.
- [24] Yamashita S, Yoshikuni Y, Obayashi H, Suzuki T, Green D, Hirata T: Simultaneous determination of size and position of silver and gold nanoparticles in onion cells using laser ablation-ICP-MS. *Anal. Chem* 91(7): 4544-4551, 2019.
- [25] Metarapi D, Šala M, Vogel-Mikuš K, Šelih VS, Van Elteren JT: Nanoparticle analysis in biomaterials using laser ablation–single particle–inductively coupled plasma mass spectrometry. *Anal. Chem* 91: 6200-6205, 2019.
- [26] Nordhorn ID, Dietrich D, Verlemann C, Vennemann A, Schmid R, Elinkmann M, Fuchs J, Sperling M, Wiemann M, Karst U: Spatially and size-resolved analysis of gold nanoparticles in rat spleen after intratracheal instillation by laser ablation-inductively coupled plasma-mass spectrometry. *Metallomics* 13: 2021, mfab028.
- [27] Sakata S, Hattori K, Iwano H, Yokoyama TD, Danhara T, Hirata T: Determination of U–Pb ages for young zircons using laser ablation-ICP-mass spectrometry coupled with an ion detection attenuator device. *Geostand. Geoanal. Res* 38(4): 409-420, 2014.
- [28] Yamashita S, Miyake A, Hirata T: Size analysis of large-sized gold nanoparticles using single particle ICP-mass spectrometry. *J. Anal. At. Spectrom* 35: 2834-2839, 2020.
- [29] Benesova I, Dlabkova K, Zelenak F, Vaculovic T, Kanicky V, Preisler J: Direct analysis of gold nanoparticles from dried droplets using substrate-assisted laser desorption single particle-ICPMS. *Anal. Chem* 88(5): 2576-2582, 2016.
- [30] Metarapi D, Van Elteren JT, Šala M: Studying gold nanoparticle degradation during laser ablation–single particle-inductively coupled plasma mass spectrometry analysis. *J. Anal. At. Spectrom.* 2021, Advance Article.
- [31] Tuoriniemi J, Cornelis G, Hassellöv M: Size discrimination and detection capabilities of single-particle ICPMS for environmental analysis of silver nanoparticles. *Anal. Chem* 84: 3965-3972, 2012.
- [32] Metarapi D, Van Elteren JT: Fundamentals of single particle analysis in biomatrices by laser ablation-inductively coupled plasma mass spectrometry. *J. Anal. At. Spectrom* 35: 784-793, 2020.
- [33] Drescher D, Zeise I, Traub H, Guttmann P, Seifert S, Büchner T, Jakubowski N, Schneider G, Kneipp J: In situ characterization of SiO<sub>2</sub> nanoparticle biointeractions using BrightSilica. *Adv. Funct. Mater* 24(24): 3765-3775, 2014.
- [34] Arakawa A, Jakubowski N, Koellensperger G, Theiner S, Schweikert A, Flemig S, Iwahata D, Traub H, Hirata T: Quantitative imaging of silver nanoparticles and essential elements in thin sections of fibroblast multicellular spheroids by high resolution laser ablation inductively coupled plasma time-of-flight mass spectrometry. *Anal. Chem* 91: 10197-10203, 2019.
- [35] Stebounova LV, Guio E, Grassian VH: Silver nanoparticles in simulated biological media: a study of aggregation, sedimentation, and dissolution. *J Nanopart Res* 13: 233-244, 2011.
- [36] Zhong L, Yu Y, Lian H, Hu X, Fu H, Chen Y: Solubility of nano-sized metal oxides evaluated by using in vitro simulated lung and gastrointestinal fluids: implication for health risks. *J Nanopart Res* 19: 375, 2017.
- [37] Laborda F, Jiménez-Lamana J, Bolea E, Castillo JR: Selective identification, characterization and determination of dissolved silver(I) and silver nanoparticles based on single particle detection by inductively coupled plasma mass spectrometry. *J. Anal. At. Spectrom* 26: 1362-1371, 2011.
- [38] Suzuki T, Yamashita S, Yoshikuni Y, Hirata T: Development of data analysis software for nanoparticle measurements by ICP-mass spectrometry. *J. Mass Spectrom. Soc. Jpn* 67: 147-153, 2019.
- [39] Makino Y, Kuroki Y, Hirata T: Determination of major to trace elements in metallic materials based on the solid mixing calibration method using multiple spot-laser ablation-ICP-MS. *J. Anal. At. Spectrom* 34: 1794-1799, 2019.
- [40] Huang HK, Wu SC: The evaluation of mass densities of the human body in vivo from CT scans. *Comput. Biol. Med. Pergamon Press* 6: 337-343, 1916.
- [41] Bryan AK, Hecht VC, Shend W, Payer K, Grover WH, Manalis SR: Measuring single cell mass, volume, and density with dual suspended microchannel resonators. *Lab Chip* 14(3): 569-576, 2014.
- [42] Singh RP, Ramarao P: Cellular uptake, intracellular trafficking and cytotoxicity of silver nanoparticles. *Toxicol Lett* 213: 249-259, 2012.
- [43] Navarro E, Piccapietra F, Wagner B, Marconi F, Kaegi R, Odzak N, Sigg L, Behra R: Toxicity of silver nanoparticles to *Chlamydomonas reinhardtii*. *Environ. Sci. Technol* 42(23): 8959-8964, 2008.
- [44] El Badawy AM, Luxton TP, Silva RG, Scheckel KG, Suidan MT, Tolaymat TM: Impact of environmental conditions (pH, ionic strength, and electrolyte type) on the surface charge and aggregation of silver nanoparticles suspensions. *Environ. Sci. Technol* 44: 1260-1266, 2010.
- [45] Stebounova LV, Guio G, Grassian VH: Silver nanoparticles in simulated biological media: a study of aggregation, sedimentation, and dissolution. *J Nanopart Res* 13: 233-244, 2011.

- [46] Johnston HJ, Hutchison G, Christensen FM, Peters S, Hankin S, Stone V: A review of the in vivo and in vitro toxicity of silver and gold particulates: particle attributes and biological mechanisms responsible for the observed toxicity. *Critical Reviews in Toxicology* 40: 328-346, 2010.
- [47] Hirn S, Semmler-Behnke M, Schleh C, Wenk A, Lipka J, Schäffler M, Takenaka S, Möller W, Schmid G, Simon U, Kreyling WG: Particle size-dependent and surface charge-dependent biodistribution of gold nanoparticles after intravenous administration. *European Journal of Pharmaceutics and Biopharmaceutics* 77: 407-416, 2011.